Journal of Intelligent Material Systems and Structures
http://jim.sagepub.com/

Experiment and Analysis of Fluidic Flexible Matrix Composite (F^2MC) Tube

Yijin Chen, Jian Sun, Yanju Liu and Jinsong Leng

Journal of Intelligent Material Systems and Structures published online 11 September 2011
DOI: 10.1177/1045389X11420591

The online version of this article can be found at:
http://jim.sagepub.com/content/early/2011/09/08/1045389X11420591

Published by:
SAGE
http://www.sagepublications.com

Article

Journal of Intelligent Material Systems and Structures

Journal of Intelligent Material Systems and Structures
XX(X) 1–12

DOI: 10.1177/1045389X11420591
jim.sagepub.com
SAGE

Experiment and Analysis of Fluidic Flexible Matrix Composite (F^2MC) Tube

Yijin Chen[1], Jian Sun[1], Yanju Liu[2] and Jinsong Leng[1]

Abstract

In this research, a fluidic flexible matrix composites (F^2MC) tube composed of flexible matrix composite (FMC) and inner liner is investigated. Significant changes in effective axial elastic modulus could be achieved through controlling the interior fluid. Based on classical laminated-plate theory and anisotropic elasticity, a three-dimensional analytical method is proposed to characterize the axial mechanical behavior of the F^2MC tube. In comparison with the experiment result, the analysis is deemed to possess satisfying accuracy in the effective axial elastic modulus prediction of the F^2MC tube. In addition, the effective axial elastic modulus ratio is discussed under different material and geometry parameters of the tube. The analysis result shows that the modulus ratio can reach up to 120 by refining the material and geometry parameters. Therefore, the investigated F^2MC tube could serve as potential candidate for the morphing skin applications with variable stiffness.

Keywords

variable stiffness, morphing skin, flexible matrix composites, classical laminated-plate theory, anisotropic elasticity

Introduction

Traditionally, aircrafts are designed according to their special mission, flight altitude, Mach number, and flight weight and usually optimized in the most concerned flight performance. However, in an integrated flight cycle with continuously varied flight parameters, the geometry of wings is not always optimal. In view of these, morphing aircrafts are designed to solve this problem (Bubert et al., 2010; Thill et al., 2008), and the recently emerged smart materials and their composites open an avenue to the development of morphing aircrafts. Morphing aircrafts can realize the optimal objective through changing its aerodynamic layout according to the outside flight environment. One of the key techniques to realize morphing aircraft is the morphing skin (Bartley-Cho et al., 2004), which should endure enough deformation if significant changes of chord length, span length, sweepback angle, and wing area are accomplished by the aircraft wing, as well as possessing enough out-of-plane stiffness to maintain the aerodynamics configuration during the deformation process. Meanwhile, to reduce the energy consumption of actuators, low in-plane stiffness is desired during the deformation process (Murray et al., 2010; Reich et al., 2007; Yin et al., 2008).

Currently, one of the main methods to realize the deformation function of the morphing skin is achieved by slide structures, such as traditional stiff skin of fish scales (Long et al., 1996). While this kind of material can meet the demand of aircraft wing on stress-bearing capability and deformation, it cannot meet the demand of smooth surface and entire air tightness and subsequently cause the poor aerodynamic efficiency of the morphing wing. Another method to realize the function is achieved by the material itself, such as rubbery materials with higher flexibility and elasticity (Andersen et al., 2007). Even though this kind of skin can satisfy the requirement of deformation and air tightness, the entire stress-bearing capability of the aircraft wing is decreased because of low stiffness and stretch of the material. Another type of material applied in this realm is shape-memory polymers (SMPs; Perkins et al., 2004; Yin et al., 2008), which exhibit a large deformation capability when its elastics modulus is low at high

[1]Centre for Composite Materials, Science Park of Harbin Institute of Technology, Harbin, P.R. China
[2]Department of Aerospace Science and Mechanics, Harbin Institute of Technology, Harbin, P.R. China

Corresponding author:
Jinsong Leng, Centre for Composite Materials, No. 2 YiKuang Street, Science Park of Harbin Institute of Technology, Harbin, P.O. Box 3011, P.R. China.
Email: lengjs@hit.edu.cn

temperature. But the limited stress-bearing capability and difficult control of heating temperature hinder their further applications.

Recently, a new kind of variable stiffness skin was proposed to solve these problems (Philen et al., 2006, 2007). The skin is integrated by flexible matrix and variable stiffness tube. While the variable stiffness skin exhibits high out-of-plane stiffness, it can undergo large strain and has low in-plane stiffness. One of the key components is the variable stiffness tube, namely, fluidic flexible matrix composites (F^2MC) tube. The F^2MC tube was first proposed by Shan et al. (Philen et al., 2006; Shan et al., 2007), and it would experience a large axial stiffness increase when the valves are closed. Utilizing elasticity solution of homogenous isotropic cylinder and Lekhnitskii's elasticity solution for a homogenous orthotropic cylinder, they also developed a three-dimensional (3D) analytical model (Shan et al., 2009) to characterize the axial stiffness behavior of a single F^2MC tube. The model prediction shows a good agreement with the experiment result. And based on this model, they briefly analyze the influence of bulk modulus of fluid, elastic modulus, and thickness of inner liner to the axial effective stiffness. In this regard, by applying classical laminated-plate theory and three-dimensional (3D) anisotropic elasticity (Bakaiyan et al., 2009; Xia et al., 2001a, b), a different 3D analytical method is proposed in this study to characterize the axial stiffness behavior of a single F^2MC tube. The derivation process of the elasticity solution theory is relatively simple. In addition, the influencing factors of fiber volume fraction of the outer flexible matrix composite (FMC) tube, Poisson's ratio of inner liner, thickness of fluid, and outer FMC tube are taken into account to determine the change of axial effective stiffness of the investigated tube. The analysis results could provide relatively comprehensive references for design and fabrication of the F^2MC tube.

Analysis Procedure

Model of the F^2MC Tube

The F^2MC tube is manufactured by filament-wound FMC laminate for the outer tube and rubber material for the inner liner (Shan et al., 2007). The outer material of the F^2MC tube is considered to be homogenous orthotropic, which has an opposite fiber orientation ($\pm\phi$) with respect to the axial direction of the rube. The outer FMC laminate is perfectly bonded to the inner liner and forms the F^2MC tube as shown in Figure 1. Through controlling the fluid inside the inner liner by valve, axial stiffness of the F^2MC tube will vary over a large interval. The entire F^2MC tube is uniformly stretched to a strain of ε_0 with an applied load of F_{ex}. As a result, a pressure of P is developed in the enclosed fluid.

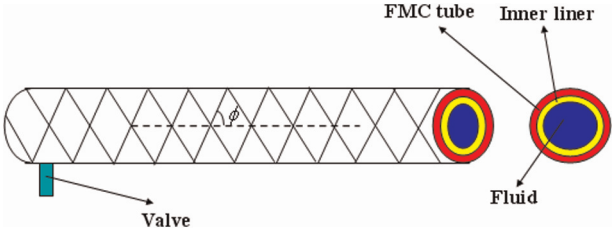

Figure 1. Illustration of the F^2MC tube.

Stress and Strain Analysis of the F^2MC Tube

Consider the F^2MC cylindrical tube subjected to an internal pressure load and an axial load as shown in Figure 2. The cylindrical coordinate system is constructed for a convenient analysis, and the coordinates are denoted by r as the radial, θ as the hoop, and z as the axial coordinates of the cylinder. When tubes are subjected to axisymmetric load, the stress and strain are independent of θ. With the assumption mentioned previously, the displacement field can be expressed as (Xia et al., 2001a)

$$u_r = u_r(r), \quad u_\theta = u_\theta(r, z), \quad u_z = u_z(z) \tag{1}$$

where u_r, u_θ, and u_z are radial, hoop, and axial displacements, respectively.

For the anisotropic materials, the stress and strain transformation of the kth layer from material coordinate to cylindrical coordinate is given by

$$\begin{Bmatrix} \sigma_z \\ \sigma_\theta \\ \sigma_r \\ \tau_{\theta r} \\ \tau_{zr} \\ \tau_{z\theta} \end{Bmatrix}^{(k)} = \begin{bmatrix} \overline{C}_{11} & \overline{C}_{12} & \overline{C}_{13} & 0 & 0 & \overline{C}_{16} \\ \overline{C}_{12} & \overline{C}_{22} & \overline{C}_{23} & 0 & 0 & \overline{C}_{26} \\ \overline{C}_{13} & \overline{C}_{23} & \overline{C}_{33} & 0 & 0 & \overline{C}_{36} \\ 0 & 0 & 0 & \overline{C}_{44} & \overline{C}_{45} & 0 \\ 0 & 0 & 0 & \overline{C}_{45} & \overline{C}_{55} & 0 \\ \overline{C}_{16} & \overline{C}_{26} & \overline{C}_{36} & 0 & 0 & \overline{C}_{66} \end{bmatrix}^{(k)} \begin{Bmatrix} \varepsilon_z \\ \varepsilon_\theta \\ \varepsilon_r \\ \gamma_{\theta r} \\ \gamma_{zr} \\ \gamma_{z\theta} \end{Bmatrix}^{(k)} \tag{2}$$

Considering the axisymmetric properties of the system and Equation (1), the strain–displacement expressions are simplified as

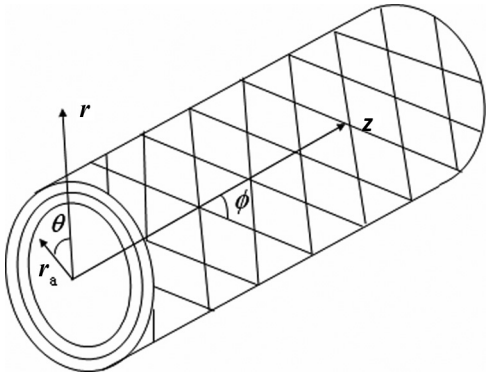

Figure 2. The F^2MC tube in cylindrical coordinate system.

$$\varepsilon_r^{(k)} = \frac{\mathrm{d}u_r^{(k)}}{\mathrm{d}r}, \quad \varepsilon_\theta^{(k)} = \frac{u_r^{(k)}}{r}, \quad \varepsilon_z^{(k)} = \frac{\mathrm{d}u_z^{(k)}}{\mathrm{d}z} = \varepsilon_0 \tag{3}$$

$$\gamma_{zr}^{(k)} = 0, \quad \gamma_{\theta r}^{(k)} = \frac{\mathrm{d}u_\theta^{(k)}}{\mathrm{d}r} - \frac{u_\theta^{(k)}}{r}, \quad \gamma_{z\theta}^{(k)} = \frac{\mathrm{d}u_\theta^{(k)}}{\mathrm{d}z} = \gamma_0 r \tag{4}$$

The expressions of the equilibrium equations are simplified as follows:

$$\frac{\mathrm{d}\sigma_r^{(k)}}{\mathrm{d}r} + \frac{\sigma_r^{(k)} - \sigma_\theta^{(k)}}{r} = 0 \tag{5}$$

$$\frac{\mathrm{d}\tau_{\theta r}^{(k)}}{\mathrm{d}r} + \frac{2\tau_{\theta r}^{(k)}}{r} = 0 \tag{6}$$

$$\frac{\mathrm{d}\tau_{zr}^{(k)}}{\mathrm{d}r} + \frac{\tau_{zr}^{(k)}}{r} = 0 \tag{7}$$

The solution of Equations (6) and (7) can be given as follows:

$$\sigma_{\theta r}^{(k)} = \frac{A^{(k)}}{r^2}, \quad \sigma_{zr}^{(k)} = \frac{B^{(k)}}{r^2} \tag{8}$$

According to Xia's elasticity solution for a homogenous cylinder under an internal pressure load and an axial load, the expression of displacement field can be obtained under the following two conditions (Xia et al., 2001a, b):

1. If $\beta^{(k)} \neq 0$, which is anisotropic,

$$u_r^{(k)} = D^{(k)} r^{\beta^{(k)}} + E^{(k)} r^{-\beta^{(k)}} + \frac{\alpha_1^{(k)} \varepsilon_0 r}{1 - (\beta^{(k)})^2} + \alpha_2^{(k)} \gamma_0 r^2 \tag{9}$$

2. If $\beta^{(k)} = 0$, which is isotropic or isotropic in $(r - \theta)$ plane,

$$u_r^{(k)} = D^{(k)} r^{\beta^{(k)}} + E^{(k)} r^{-\beta^{(k)}} + \frac{\alpha_1^{(k)} \varepsilon_0 r \ln r}{2} + \alpha_2^{(k)} \gamma_0 r^2 \tag{10}$$

where $\beta^{(k)} = \sqrt{\overline{C}_{22}^{(k)} / \overline{C}_{33}^{(k)}}$, $\alpha_1^{(k)} = (\overline{C}_{12}^{(k)} - \overline{C}_{13}^{(k)}) / (\overline{C}_{33}^{(k)})$, $\alpha_2^{(k)} = (\overline{C}_{26}^{(k)} - 2\overline{C}_{36}^{(k)}) / (4\overline{C}_{33}^{(k)} - \overline{C}_{22}^{(k)})$, ε_0 is the axial strain of all layers, γ_0 is the twist of tube per unit length, and $D^{(k)}$ and $E^{(k)}$ are unknown constants of integration determined from the boundary conditions.

Laminated-Plate Properties

The off-axis stiffness constants in matrix $\left[\overline{C}_{ij}^{(k)}\right]$ can be obtained from the on-axis coordinate constants in matrix $\left[C_{ij}^{(k)}\right]$ as shown in Figure 3, using a stiffness transformation matrix written as follows (Bakaiyan et al., 2009):

$$\left[\overline{C}_{ij}^{(k)}\right] = \left[T_{il}^{\sigma}\right]^{-1} \left[C_{lm}^{(k)}\right] \left[T_{mj}^{\varepsilon}\right] \tag{11}$$

where matrix $\left[T_{il}^{\sigma}\right]$ and $\left[T_{mj}^{\varepsilon}\right]$ are the base change of stress and strain, respectively, which are expressed as follows:

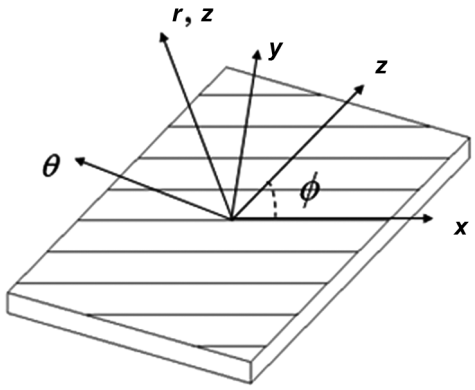

Figure 3. Coordinate relationships between principal material axis and cylindrical axis.

$$\left[T_{il}^{\sigma}\right] = \begin{bmatrix} m^2 & n^2 & 0 & 0 & 0 & 2mn \\ n^2 & m^2 & 0 & 0 & 0 & -2mn \\ 0 & 0 & 1 & 0 & 0 & 0 \\ 0 & 0 & 0 & m & -n & 0 \\ 0 & 0 & 0 & n & m & 0 \\ -mn & mn & 0 & 0 & 0 & m^2 - n^2 \end{bmatrix} \tag{12}$$

$$\left[T_{mj}^{\varepsilon}\right] = \begin{bmatrix} m^2 & n^2 & 0 & 0 & 0 & mn \\ n^2 & m^2 & 0 & 0 & 0 & -mn \\ 0 & 0 & 1 & 0 & 0 & 0 \\ 0 & 0 & 0 & m & -n & 0 \\ 0 & 0 & 0 & n & m & 0 \\ -2mn & 2mn & 0 & 0 & 0 & m^2 - n^2 \end{bmatrix} \tag{13}$$

where $m = \cos\phi$ and $n = \sin\phi$, and ϕ is the filament-wound angle from the tube axis. The stiffness constants of matrix $\left[C_{ij}^{(k)}\right]$ are given as follows:

$$\begin{aligned} \Delta &= \frac{1 - \nu_{12}\nu_{21} - \nu_{13}\nu_{31} - \nu_{23}\nu_{32} - 2\nu_{21}\nu_{13}\nu_{32}}{E_{11}E_{22}E_{33}} \\ C_{11} &= \frac{1 - \nu_{23}\nu_{32}}{E_{22}E_{33}\Delta}, \\ C_{12} &= \frac{\nu_{12} + \nu_{13}\nu_{32}}{E_{11}E_{33}\Delta}, \\ C_{13} &= \frac{\nu_{13} + \nu_{12}\nu_{23}}{E_{11}E_{22}\Delta} \\ C_{22} &= \frac{1 - \nu_{13}\nu_{31}}{E_{11}E_{33}\Delta}, \\ C_{23} &= \frac{\nu_{23} + \nu_{21}\nu_{13}}{E_{11}E_{22}\Delta}, \\ C_{33} &= \frac{1 - \nu_{12}\nu_{21}}{E_{11}E_{22}\Delta} \\ G_{44} &= G_{23}, \quad G_{55} = G_{31}, \quad G_{66} = G_{12} \end{aligned} \tag{14}$$

While each layer of the laminated-plate exhibits the properties of fiber-reinforced composite materials, the matrix material is isotropic and fiber is transversely isotropic, and its elastic constants can be expressed as follows (Chang et al., 2007):

$$E_{11} = V_f E_{f11} + V_m E_m, \quad E_{22} = E_{33} = \frac{E_{f22} E_m}{E_{f22} V_m + E_m V_f},$$
$$G_{12} = G_{13} = \frac{G_{f12} G_m}{G_{f12} V_m + G_m V_f}$$
$$G_{23} = \frac{G_{f23} G_m}{G_{f23} V_m + G_m V_f}, \quad v_{12} = v_{13} = V_f v_{f12} + V_m v_m,$$
$$v_{23} = V_f v_{f23} + V_m v_m \tag{15}$$

where E_{f11}, E_{f22}, G_{f12}, G_{f23}, v_{f12}, and v_{f23} are the material constants of fiber; E_m, v_m, and G_m are the material constants of matrix; and V_f and V_m are the volume fraction of fiber and matrix material.

Boundary Conditions

It is assumed that the stress and displacement field are continuous. All the unknown constants in stress, strain, and displacement expressions will be determined by the boundary conditions. The stress boundary conditions on both inner and outer surfaces are expressed as follows (Xia et al., 2001a):

$$\sigma_r^{(1)}(r_a) = -P, \quad \sigma_r^{(n)}(r_b) = 0, \quad \tau_{zr}^{(1)}(r_a) = \tau_{\theta r}^{(1)}(r_a) = 0,$$
$$\tau_{zr}^{(n)}(r_b) = \tau_{\theta r}^{(n)}(r_b) = 0 \tag{16}$$

where r_a and r_b are the inner and outer radii, respectively.

If the outer FMC laminate and inner liner are perfectly bound, the continuity conditions for stress and displacement in the interfaces are given by

$$u_r^{(k)}(r_k) = u_r^{(k+1)}(r_k), \quad u_\theta^{(k)}(r_k) = u_\theta^{(k+1)}(r_k)$$
$$\sigma_r^{(k)}(r_k) = \sigma_r^{(k+1)}(r_k), \quad \tau_{zr}^{(k)}(r_k) = \tau_{zr}^{(k+1)}(r_k), \tag{17}$$
$$\tau_{\theta r}^{(k)}(r_k) = \tau_{\theta r}^{(k+1)}(r_k)$$

In addition, the two integral conditions can be expressed as follows:

$$2\pi \sum_{k=1}^{n} \int_{r_{k-1}}^{r_k} \sigma_z^{(k)}(r) r \, \mathrm{d}r = \pi r_a^2 P + F_{ex} \tag{18}$$

$$2\pi \sum_{k=1}^{n} \int_{r_{k-1}}^{r_k} \tau_{z\theta}^{(k)}(r) r^2 \, \mathrm{d}r = 0 \tag{19}$$

Due to internal pressure with the end loading effect for a cylinder, the first integral condition satisfies the equilibrium of axial force, and the second equation is considered to be the zero torsion condition.

According to the expression of stress boundary conditions, the unknown integration constants $A^{(k)} = B^{(k)} = 0$. For N-layered composite tube, there are $2N + 3$ unknown constants of integration, that is, $D^{(k)}$, $E^{(k)}$ ($k = 1, 2, \ldots, N$), and γ_0, P, F_{ex}. These unknown constants can be determined by $2N + 2$ equations of boundary conditions and an additional equation for compressible fluid. Assuming there is a F^{2}MC tube with N ($N = 5$) layers, $2(N + 1)$ equations can be given as follows:

$$\begin{Bmatrix} D^{(1)} \\ D^{(2)} \\ D^{(3)} \\ D^{(4)} \\ D^{(5)} \\ E^{(1)} \\ E^{(2)} \\ E^{(3)} \\ E^{(4)} \\ E^{(5)} \\ \varepsilon_0 \\ \gamma_0 \end{Bmatrix} =$$
$$\begin{bmatrix} k_{11} & k_{12} & k_{13} & k_{14} & k_{15} & k_{16} & k_{17} & k_{18} & k_{19} & k_{10} & k_{1a} & k_{1b} \\ k_{21} & k_{22} & k_{23} & k_{24} & k_{25} & k_{26} & k_{27} & k_{28} & k_{29} & k_{20} & k_{2a} & k_{2b} \\ k_{31} & k_{32} & k_{33} & k_{34} & k_{35} & k_{36} & k_{37} & k_{38} & k_{39} & k_{30} & k_{3a} & k_{3b} \\ k_{41} & k_{42} & k_{43} & k_{44} & k_{45} & k_{46} & k_{47} & k_{48} & k_{49} & k_{40} & k_{4a} & k_{4b} \\ k_{51} & k_{52} & k_{53} & k_{54} & k_{55} & k_{56} & k_{57} & k_{58} & k_{59} & k_{50} & k_{5a} & k_{5b} \\ k_{61} & k_{62} & k_{63} & k_{64} & k_{65} & k_{66} & k_{67} & k_{68} & k_{69} & k_{60} & k_{6a} & k_{6b} \\ k_{71} & k_{72} & k_{73} & k_{74} & k_{75} & k_{76} & k_{77} & k_{78} & k_{79} & k_{70} & k_{7a} & k_{7b} \\ k_{81} & k_{82} & k_{83} & k_{84} & k_{85} & k_{86} & k_{87} & k_{88} & k_{89} & k_{80} & k_{8a} & k_{8b} \\ k_{91} & k_{92} & k_{93} & k_{94} & k_{95} & k_{96} & k_{97} & k_{98} & k_{99} & k_{90} & k_{9a} & k_{9b} \\ k_{01} & k_{02} & k_{03} & k_{04} & k_{05} & k_{06} & k_{07} & k_{08} & k_{09} & k_{00} & k_{0a} & k_{0b} \\ k_{a1} & k_{a2} & k_{a3} & k_{a4} & k_{a5} & k_{a6} & k_{a7} & k_{a8} & k_{a9} & k_{a0} & k_{aa} & k_{ab} \\ k_{b1} & k_{b2} & k_{b3} & k_{b4} & k_{b5} & k_{b6} & k_{b7} & k_{b8} & k_{b9} & k_{b0} & k_{ba} & k_{bb} \end{bmatrix}^{-1}$$
$$\begin{Bmatrix} -P \\ 0 \\ 0 \\ 0 \\ 0 \\ 0 \\ 0 \\ 0 \\ 0 \\ 0 \\ \frac{\pi r_a^2 P + F_{ex}}{2\pi} \\ 0 \end{Bmatrix} \tag{20}$$

where k_{ij} are the coefficients of unknown constants and can be obtained by the equations of boundary conditions. Based on these unknown constants, the stress, strain, and displacement can be determined from equilibrium equations, strain–displacement expressions, displacement expressions, and stress–strain relationships.

Equation for Compressible Fluid

When the valve of the F^{2}MC tube is closed, the fluid inside the inner liner will be compressed with an applied load of F_{ex}. As a result, the volume of the tube will be changed by ΔV. In addition, the pressure of the enclosed fluid will be increased from zero to P. The relationship of fluid and pressure can be expressed as follows (Shan et al., 2009):

$$B\left(\frac{\Delta V}{V_0}\right) = -P \tag{21}$$

Figure 4. Filament wound of the F^{2}MC tube.

where B and V_0 are the bulk modulus and volume of the fluid, respectively. Neglecting the higher order of strain caused by compression, the expression can be simplified as

$$B\left(\varepsilon_z^{(1)}(r_a) + 2\varepsilon_\theta^{(1)}(r_a)\right) = -P \tag{22}$$

Effective Modulus and Modulus Ratio of the F^{2}MC Tube

Once these $2N + 3$ unknown constants are determined, the effective closed-valve modulus of E_z^{close} and open-valve modulus of E_z^{open} in the axial direction is defined as (Shan et al., 2007)

$$E_z^{close} = \frac{F_{ex}^{close}}{\pi r_b^2 \varepsilon_0}, \quad E_z^{open} = \frac{F_{ex}^{open}}{\pi r_b^2 \varepsilon_0}, \tag{23}$$

When the entire F^{2}MC tube is uniformly stretched to a target strain of ε_0, a load of F_{ex}^{close} should be applied under the closed-valve state. Similarly, a load of F_{ex}^{open} should be applied under the open-valve state, which means the pressure P is zero. Based on this fact, the effective modulus ratio R is defined as follows:

$$R = \frac{E_z^{close}}{E_z^{open}} \tag{24}$$

F^{2}MC Tube Fabrication and Tensile Test

F^{2}MC Tube Fabrication

The F^{2}MC tube was wet filament wound using a computer-controlled filament-winding machine (SKLCR 120/500, Qier Machine Tool Group Co., Ltd.) as shown in Figure 4. Before filament winding, a thin rubber inner liner is placed on the mandrel and then the two ends of the mandrel were fixed by three-jaw chucks with stainless steel connections. The carbon fiber (T300, 3K) was winded on the mandrel at $\pm\phi$ angle through the control of computer. The uncured silicone raw material was brushed on the surface of the mandrel during the filament-wound procedure. After curing at the room temperature for 35 h, the F^{2}MC tube specimen was obtained as shown in Figure 5, with a fiber volume fraction of the outer FMC tube of 0.7.

Figure 5. The F^{2}MC tube specimens.

Tensile Test

In this session, the F^{2}MC tubes with a length of 160 mm, an outer diameter of 7.8 mm, and an inner diameter of 5 mm were tested to investigate their mechanical properties at two states: closed valve and open valve. Two hydraulic fittings with right size were inserted and glued with epoxy glue to both ends of the tube. In order to ensure the fluid tightness and sustain large axial loads, two stainless steel clamp collars were placed on the surface of the two ends to clamp the tube and hydraulic fittings together. Two screw plugs will be screwed into the hydraulic fittings after the fluid is filled with the tube to achieve the closed-valve condition. Tensile test was performed at 25°C at a constant rate of 2 mm/min on a Materials Testing Machine (T1-FR050TH A1K, ZWICK), as shown in Figure 6. The values of force and displacement were recorded using the computer during the tensile test.

Results and Discussion

Elastic Constants of FMC Layer

The basic material and geometry parameters of fiber and matrix are listed in Table 1. If each layer of FMC laminate is considered to be fiber-reinforced composite, their elastic constants with different fiber volume fractions can be obtained by substituting the parameters into Rule of Mixture expression of Equation (15).

Experiment and Analysis Result of a Single F^{2}MC Tube

The experimental setup for tensile test of the F^{2}MC tube is shown in Figure 6. The fiber volume fraction of the outer FMC tube is 0.7 and the filament-wound

Table 1. Basic material and geometry parameters of fiber and matrix.

Material	Property	Value	Geometry	Value
Carbon fiber (T300)	E_{11} (GPa)	221	Length of FMC (mm)	160
	E_{22} (GPa)	13.8		
	G_{12} (GPa)	9		
	v_{12}	0.2	Inner diameter of FMC (mm)	7
	v_{23}	0.25		
Matrix (silicone)	E_m (MPa)	1.4	Outer diameter of FMC (mm)	7.8
	v_m	0.49		
Inner liner	E (MPa)	0.1	Inner diameter (mm)	5
	V	0.497	Outer diameter (mm)	7
Fluid	B (GPa)	2	Outer diameter (mm)	5

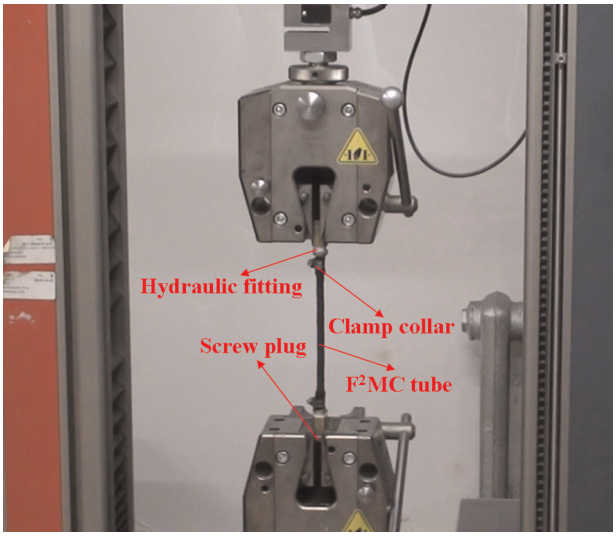

Figure 6. The F²MC tube experiment setup.

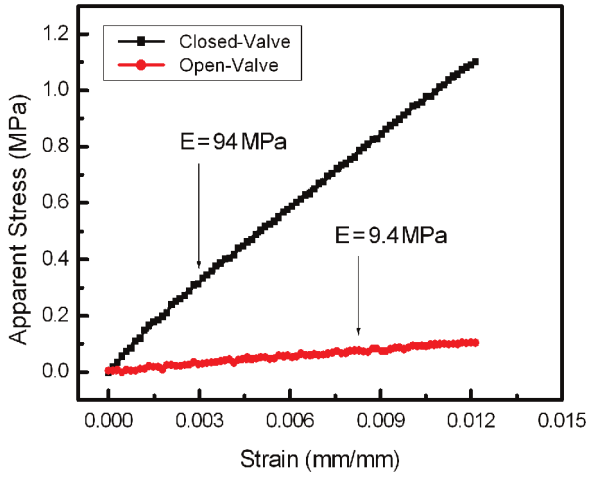

Figure 7. Experiment curves of apparent stress versus strain of the F²MC tube.

angle is ±35°. The apparent stress in the figure is calculated as the tensile force divided by the entire cross-sectional area of the F²MC tube. The strain is approximated as the displacement divided by the original length of the F²MC tube. The curve of apparent stress versus strain is depicted in Figure 7. In order to exactly describe the actual situation, a F²MC tube with N (N = 3, 5, 7) layers is assumed in the analysis procedure. The effective modulus and modulus ratio are compared with the reference study (Shan et al., 2007) and experiment result, as shown in Table 2. The comparison shows that the developed 3D analytical method can describe the experiment result accurately when the layer N is higher than 5. In order to maintain the accuracy of a 3D analytical method and simplify the calculation process, seven layers of F²MC tube is constructed in the following analysis procedure.

Analysis and Discussion of a F²MC Tube with Different Conditions

Fiber Volume Fraction. To further reveal the effect of fiber volume fraction on the effective modulus and modulus ratio, a series of curves about modulus and modulus ratio under the states of closed valve and open valve are shown in Figures 8 and 9. Only one of the material and geometry parameters has been discussed for each time, while other parameters remain constant. In order to show that the analysis results of this study and the reference (Shan et al., 2007) are comparable, the basic material and geometry parameters of Figures 8 and 9 are obtained based on the data shown in Table 3, except the property values of FMC lamina that are replaced by the carbon fiber (T300) and matrix (silicone) in Table 1. It is observed from Figure 8(a) that when the fiber volume fraction is a constant, the closed-valve modulus exhibits a trend of decrease first and then increases with the increase in fiber angle. The minimum value appears at the point where fiber-winding angle is 55° , which has also been certified by the description of Philen et al. (2006). This phenomenon is mainly attributed to the reason that 55° fiber-winding angle is the boundary point of positive and negative internal pressures resulted from the tensile axial force. A negative change in internal pressure will be resulted from the tensile axial force for fiber-winding angle higher than 55°, and a positive change in internal

Table 2. Effective modulus and modulus ratio results: Analysis and experiment.

	Closed-valve modulus (MPa)	Open-valve modulus (MPa)	Modulus ratio
$N = 3$	92.493	6.0937	15.178
$N = 5$	92.531	7.2704	12.727
$N = 7$	92.538	7.4686	12.39
Reference	92.544	7.6273	12.133
Experiment	94	9.4	10

pressure for fiber-winding angle lower than 55°. In this manner, a fiber-winding angle of 55° should be the point where no pressure is produced. Besides, the closed-valve modulus increases along with the increase in fiber volume fraction when the fiber-winding angle is a constant. Similar phenomenon exists in the curves of Figure 8(b). It can also be found from Figure 8(b) that when the fiber volume fraction is a constant, the open-valve modulus decreases rapidly for the fiber-winding angle lower than 55° and approaches to a constant for the fiber-winding angle higher than 55° with the increase in fiber-winding angle. Figure 9 indicates that the maximum modulus ratio can change from 20 to 80 with different fiber volume fractions. The maximum modulus ratio increases with the decreasing fiber volume fraction, but the increase in range becomes less and less.

Fluid (Bulk Modulus B and Radius t_1). In order to compare the analysis result with reference, the basic material and geometry parameters in the following discussions will be fitted the same value as those in reference (Shan et al., 2007), as shown in Table 3. As one of the component parts, the material and geometry properties of fluid play an important role in the stiffness variation of the F^2MC tube. The variable stiffness ability of the F^2MC tube is mainly due to the high bulk modulus of fluid and the high anisotropy of the FMC tube. The curves of closed-valve and open-valve moduli versus fiber angle of the F^2MC tube with different bulk moduli of fluid are shown in Figure 10(a). It is revealed that when the bulk modulus is a constant, the closed-valve and open-valve moduli exhibit a trend of first decreasing rapidly and then increasing slowly along with the increase in fiber angle. The closed-valve modulus increases along with the increase in bulk modulus when fiber-winding angle is a constant. Considering that the variation of bulk modulus has no effect on the open-valve modulus, only one bulk modulus is shown in Figure 10(a) under open-valve condition. The relationship between the modulus ratio and fiber angle of the F^2MC tube with different bulk moduli of fluid is depicted in Figure 10(b). Along with the increase in bulk modulus, the maximum modulus ratio has greatly increased. The modulus ratio does not increase remarkably when the bulk modulus is larger than 500 MPa. In addition, the change in phenomenon of modulus ratio in Figure 10(b) based on this study fits exactly with the corresponding results that are demonstrated in the reference (Shan et al., 2007).

Figure 11(a) shows the curves of closed-valve and open-valve moduli versus fiber angle of the F^2MC tube with different radii of fluid. It is revealed that the closed-valve modulus increases along with the increase in radius when fiber-winding angle is a constant. It is mainly attributed to the relative increase of the fluid volume and the relative decrease of the inner liner volume and FMC tube volume. Moreover, such change of

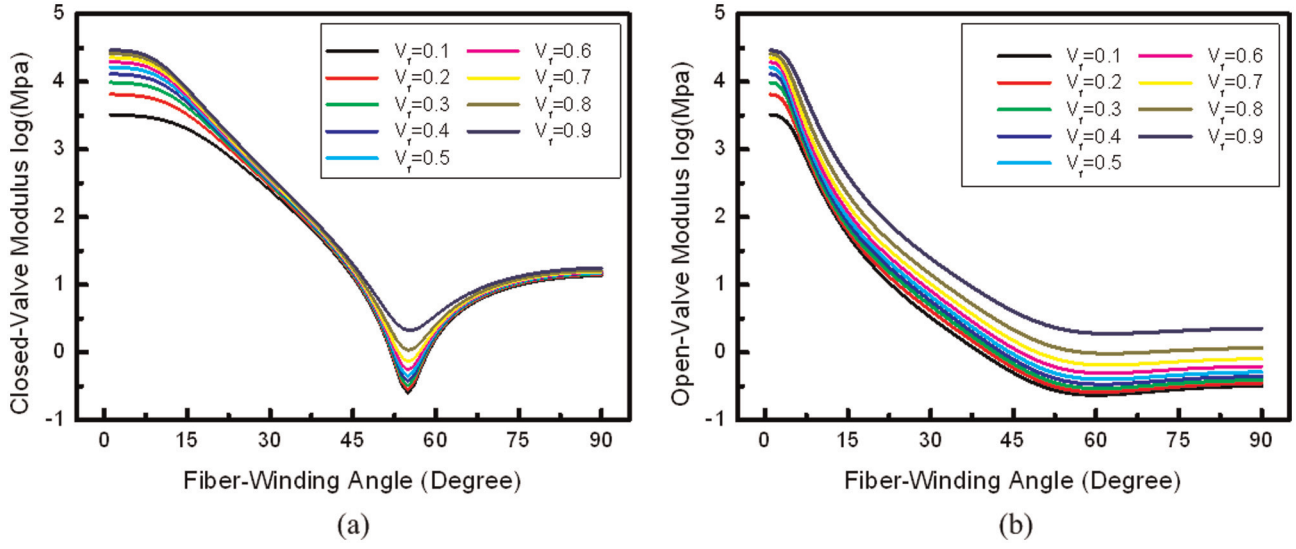

Figure 8. Curves of modulus versus fiber angle of the F^2MC tube with different fiber volume fractions: (a) closed-valve modulus and (b) open-valve modulus.

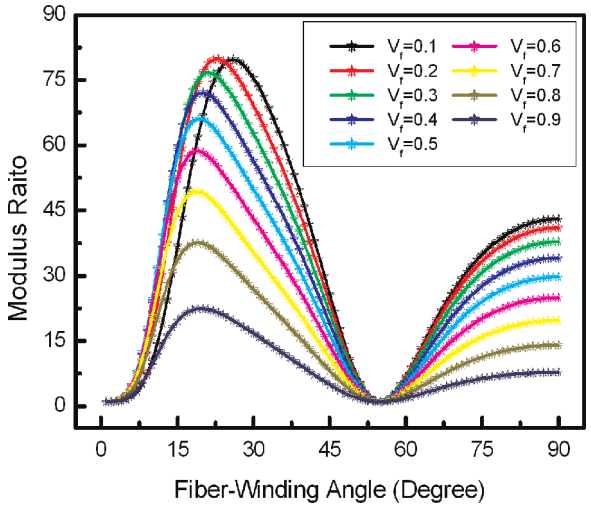

Figure 9. Curves of modulus ratio versus fiber angle of the F^2MC tube with different fiber volume fractions.

Table 3. Basic material and geometry parameters in reference.

Material	Property	Value
FMC lamina	E_{11} GPa)	115
	E_{22} (MPa)	1.8
	G_{12} (MPa)	1.4
	v_{12}	0.33
	v_{23}	0.93
Inner liner	E (MPa)	0.1
	v	0.497
Fluid	B (GPa)	2
Geometry	Outer diameter of fluid (mm)	10
	Outer diameter of inner liner (mm)	12
	Outer diameter of FMC (mm)	13

relative volume has a positive effect on the increase in closed-valve modulus. However, the open-valve modulus decreases with the increase in radius. The main reason of such result is the decreased volume fraction of the FMC tube. The relationship between the modulus ratio and fiber angle of the F^2MC tube with different radii of fluid is depicted in Figure 11(b). Along with the increase in radius, the maximum modulus ratio is uniformly increased when the radius is a constant. With the radius changing from 3 to 7 mm, the maximum modulus ratio reaches up to 120.

Inner Liner (Elastic Modulus E, Thickness t_2, and Poisson's Ratio v). The primary function of inner liner is to prevent fluid from leakage, and its material and geometry parameter change also plays a significant role on the modulus and modulus ratio. As an isotropic material, the elastic modulus of inner liner should be first considered. The curves of closed-valve and open-valve moduli versus fiber angle of the F^2MC tube with different elastic moduli of inner liner are shown in Figure 12(a). As seen in Figure 12(a), both closed-valve and open-valve moduli are increased with the increase in elastic modulus of inner liner while the fiber-winding angle is a constant. The relationship between the modulus ratio and fiber angle of the F^2MC tube with different elastic moduli of inner liner is depicted in Figure 12(b). Along with the increase in elastic modulus, the maximum modulus ratio presents the trend of first increases and then decreases. Along with the increase in the inner liner modulus, it will be more difficult to compress the inner liner under closed-valve state, and then a high modulus ratio is obtained, which results from the generated high internal pressure. However, the high

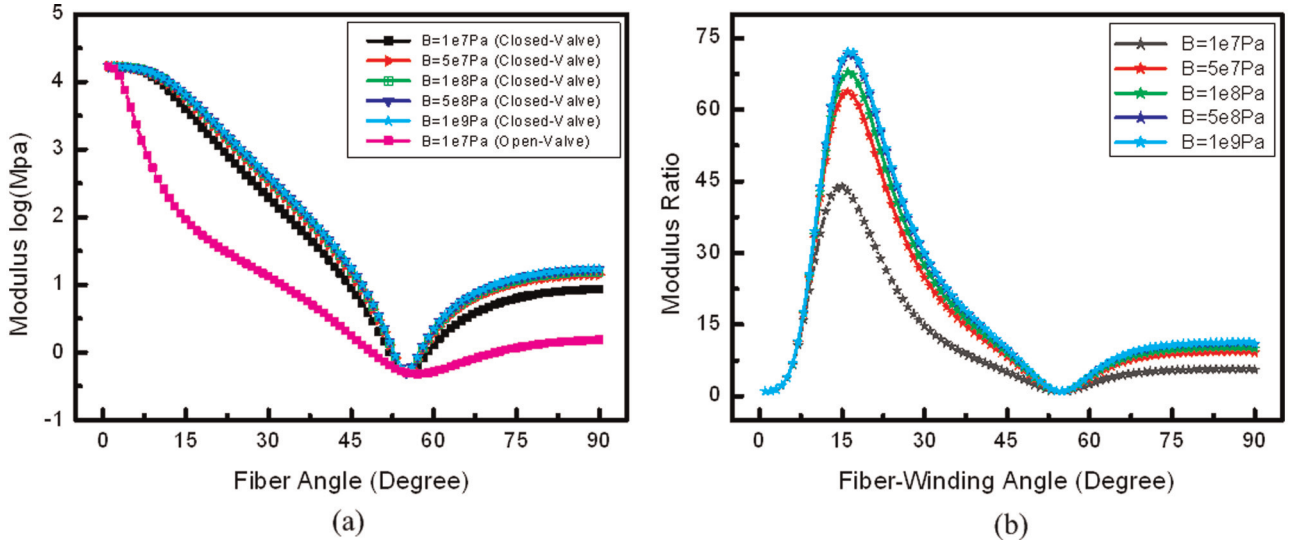

Figure 10. Curves of modulus versus fiber angle of the F^2MC tube with different bulk moduli of fluid: (a) closed-valve and open-valve moduli and (b) modulus ratio.

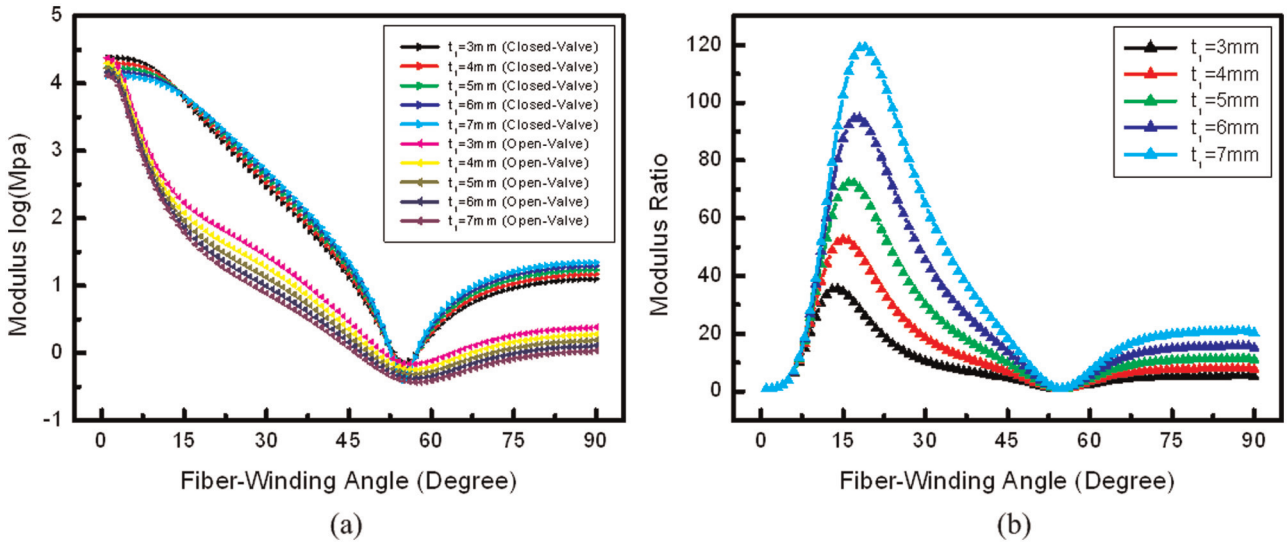

Figure 11. Curves of modulus versus fiber angle of the F^{2}MC tube with different radii of fluid: (a) closed-valve and open-valve moduli and (b) modulus ratio.

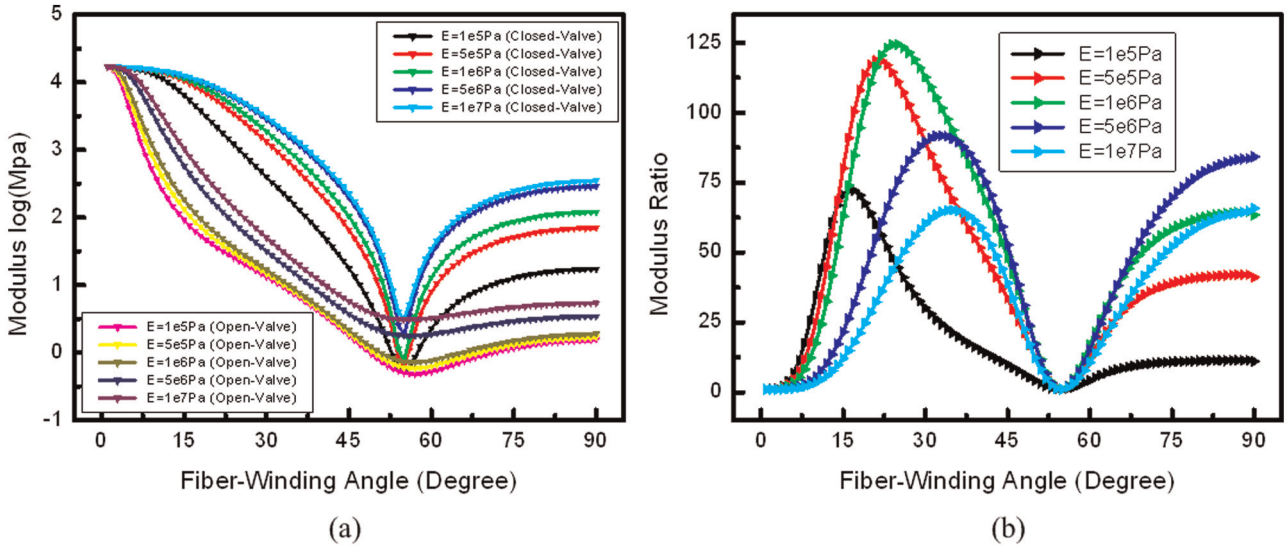

Figure 12. Curves of modulus versus fiber angle of the F^{2}MC tube with different elastic moduli of inner liner: (a) closed-valve and open-valve moduli and (b) modulus ratio.

modulus ratio will decrease along with the increase in the open-valve modulus, which results from the excessive increase in inner liner modulus. In addition, the change in regularity of modulus ratio in Figure 12(b) based on this study fits exactly with the corresponding results in the reference (Shan et al., 2007).

Figure 13(a) shows the curves of closed-valve and open-valve moduli versus fiber angle of the F^{2}MC tube with different thicknesses of inner liner. Both the closed-valve and open-valve moduli decrease with the increase in thickness of inner liner when fiber-winding angle is a constant. For the modulus of the inner liner is far lower than the fluid, it will be more easy to compress the inner liner under closed-valve state. As a result, the increase in the thickness of inner liner results in a more volume reduction of inner liner under high internal pressure, causing the closed-valve modulus to decrease. The relation between the modulus ratio and fiber angle of the F^{2}MC tube with different thicknesses of inner liner is depicted in Figure 13(b). It can be observed that the smaller the thickness of inner liner, the larger the maximum modulus ratio is. Therefore, in order to improve the modulus ratio of the F^{2}MC tube, it is important to decrease the thickness of inner liner.

The curves of closed-valve and open-valve moduli versus fiber angle of the F^{2}MC tube with different

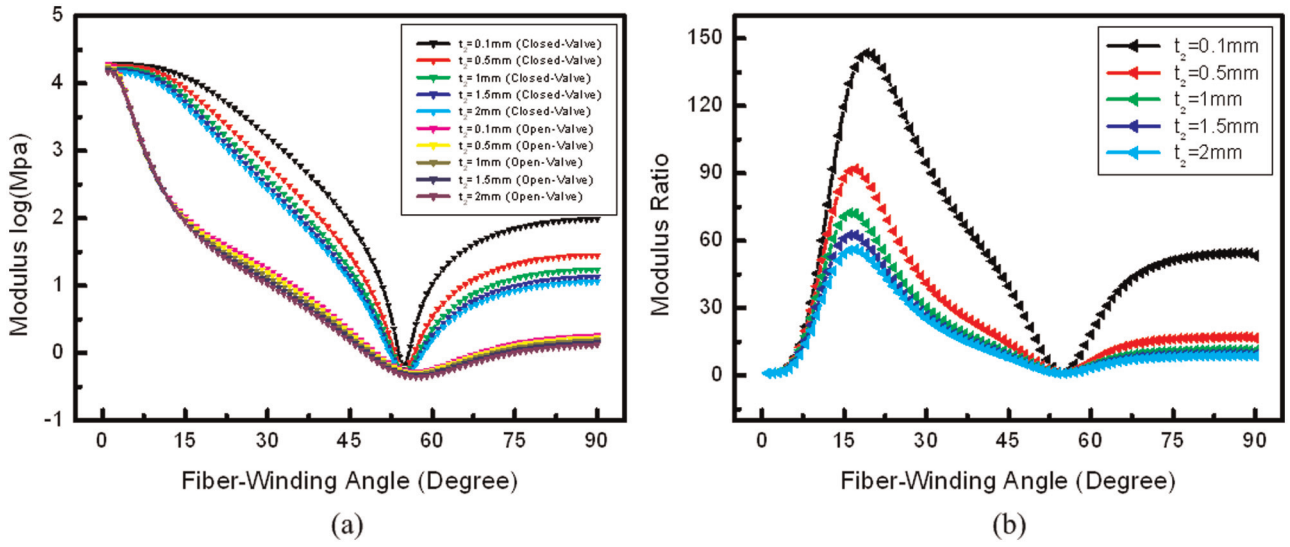

Figure 13. Curves of modulus versus fiber angle of the F^2MC tube with different thicknesses of inner liner: (a) closed-valve and open-valve moduli and (b) modulus ratio.

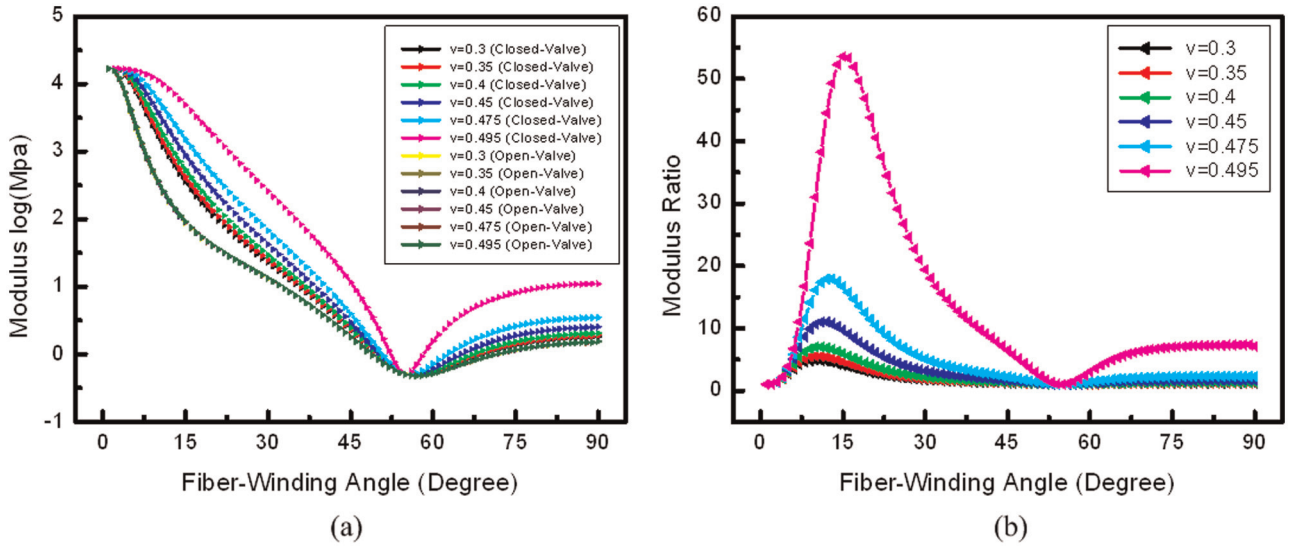

Figure 14. Curves of modulus versus fiber angle of the F^2MC tube with different Poisson's ratios of inner liner: (a) closed-valve and open-valve moduli and (b) modulus ratio.

Poisson's ratios of inner liner are shown in Figure 14(a). It can be found that the increase in Poisson's ratio plays a positive contribution to the increase in the closed-valve modulus, that is, the increase in Poisson's ratio makes no difference to the open-valve modulus. As seen in the curves of modulus ratio versus fiber angle of the F^2MC tube with different Poisson's ratios of inner liner in Figure 14(b), the maximum modulus ratio increases with the increase in Poisson's ratio. Within the variation range of Poisson's ratio, the increasing speed of modulus ratio for the Poisson's ratio more than 0.475 is larger than that for the Poisson's ratio less than 0.475.

Outer FMC Tube (Thickness t_3). As mentioned previously, one of the primary reasons resulting in the ability of variable stiffness is the high anisotropy of the FMC tube. Clearly, thickness should be one of the factors that has an effect on the modulus ratio of the F^2MC tube. For simplicity, only thickness of the outer FMC tube is discussed in this section. The curves of closed-valve and open-valve moduli versus fiber angle of the F^2MC tube with different thicknesses of the outer FMC tube are shown in Figure 15(a). Along with the increase in the thickness of the outer FMC tube, the open-valve modulus increases when the fiber-winding angle is a constant. But there is no significant change

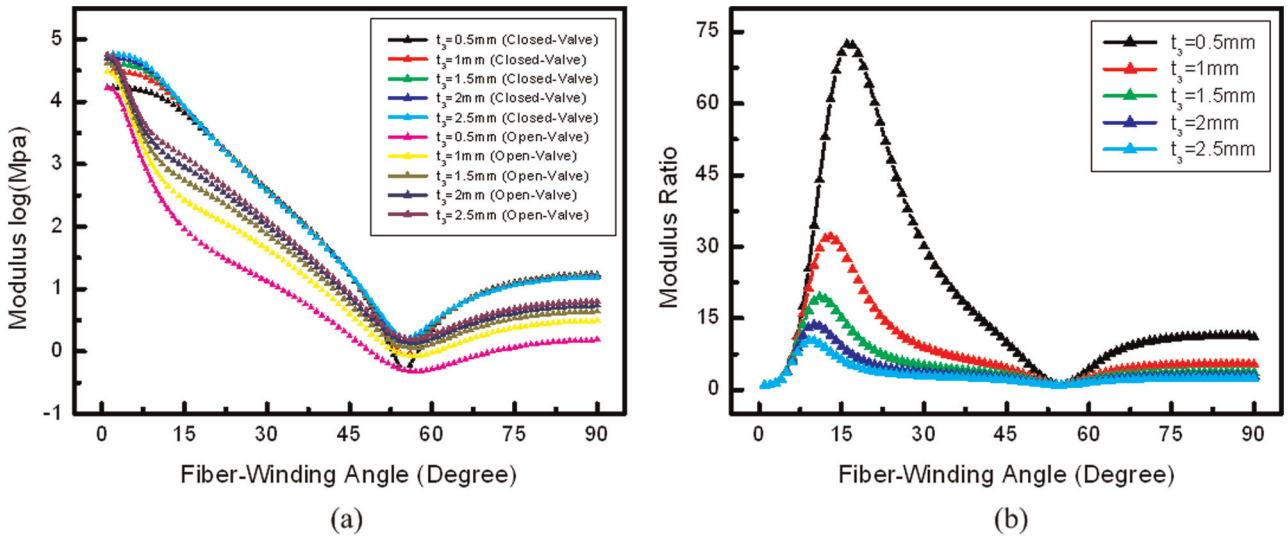

Figure 15. Curves of modulus versus fiber angle of the F^{2}MC tube with different thicknesses of the outer FMC tube: (a) closed-valve and open-valve moduli and (b) modulus ratio.

about the closed-valve modulus during the process mentioned previously. It is mainly attributed to the reason that the outer FMC tube will play an important role in the open-valve state and the compressive fluid in the closed-valve state. The relationship between the modulus ratio and fiber angle of the F^{2}MC tube with different thicknesses of the outer FMC tube is depicted in Figure 15(b). It can be observed that the smaller the thickness of the outer FMC tube, the larger the maximum modulus ratio. The variation of modulus ratio is similar to that shown in Figure 13(b). Therefore, it is necessary to decrease the thickness of the outer FMC tube to improve the performance of the F^{2}MC tube.

Conclusion

To conclude, a F^{2}MC tube with remarkably variable stiffness is manufactured and analyzed in this research. Significant changes of effective axial elastic modulus can be achieved through controlling the interior fluid by valve. A 3D analytical method based on classical laminated-plate theory and anisotropic elasticity is proposed to characterize the axial stiffness behavior of the F^{2}MC tube. The established elasticity solution theory is easily derived and is utilized to analyze the influence of various material and geometry parameters to the axial effective stiffness. Comparison between the calculation results and the references shows that the 3D analytical method can describe the tensile test result accurately when the layer number is more than 5. Besides, it is also found that the modulus ratio can be significantly changed by adjusting the material and geometry parameters of the F^{2}MC tube. The presented analysis provides meaningful guidance to assist design and manufacture of F^{2}MC tubes in variable stiffness skin applications.

Acknowledgment

This research is sponsored by the National Natural Science Foundation of China (Grant Nos. 50830201/E0503, 90916011, and 90816026). The authors wish to acknowledge it and Harbin Institute of Technology.

References

Andersen GR, Cowan DL and Piatak DJ (2007) Aeroelastic modeling, analysis and testing of a morphing wing structure. *Proceedings 48th AIAA/ASME/ASCE/AHS/ASC Structures, Structural Dynamics, and Materials Conference*, Honolulu, Hawaii.

Bakaiyan H, Hosseini H and Ameri E (2009) Analysis of multi-layered filament-wound composite pipes under combined internal pressure and thermomechanical loading with thermal variations. *Composite Structures* 88(4): 532–541.

Bartley-Cho JD, Wang DP, Martin CA, Kudva JN and West MN (2004) Development of high-rate, adaptive trailing edge control surface for the smart wing phase 2 wind tunnel model. *Journal of Intelligent Material Systems and Structures* 15(4): 279–291.

Bubert EA, Woods BKS, Lee K, Kothera CS and Wereley NM (2010) Design and fabrication of a passive 1D morphing aircraft skin. *Journal of Intelligent Material Systems and Structures* 21(17): 1699–1717.

Chang YJ, Jiao GQ, Wang B and Liu HX (2007) Micromechanical model for elastic properties of 3D angle-interlock woven ceramic composites. *Chinese Journal of Applied Mechanics* 24(1): 146–150 (in Chinese).

Long J, Hale M, Mchenry M and Westneat M (1996) Functions of fish skin: Flexural stiffness and steady swimming of Longnose Gar Lepisosteus Osseus. *Journal of Experimental Biology* 199(10): 2139–2151.

Murray G, Gandhi F and Bakis C (2010) Flexible matrix composite skins for one-dimensional wing morphing. *Journal of Intelligent Material Systems and Structures* 21(17): 1771–1781.

Perkins DA, Reed JL and Havens JE (2004) Morphing wing structures for loitering air vehicles. *Proceedings 45th AIAA/ASME/ASCE/AHS/ASC Structures Dynamics and Materials Conference*, Palm Springs, California.

Phillen M, Shan Y, Bakis CE, Wang KW and Rahn CD (2006) Variable stiffness adaptive structures utilizing hydraulically pressurized flexible matrix composites with valve control. *47th AIAA/ASME/ASCE/AHS/ASC Structures, Structural Dynamics and Materials Conference*, Newport, Rhode Island.

Phillen M, Shan Y, Wang KW, Bakis CE and Rahn CD (2007) Fluidic flexible matrix composites for the tailoring of variable Stiffness Adaptive Structures. *Proceedings 48th AIAA/ASME/ASCE/AHS/ASC Structures, Structural Dynamics and Materials Conference*, Honolulu, Hawaii.

Reich GW, Sanders B and Joo JJ (2007) Development of skins for morphing aircraft applications via topology optimization. *Journal of Intelligent Material Systems and Structures* 20(April): 1–13.

Shan Y, Lotfi A, Phillen M, Li SY, Bakis CE, Rahn CD, et al. (2007) Fluidic flexible matrix composites for autonomous structural tailoring. *Proceedings of SPIE, the International Society for Optical Engineering* 6525: 1–14.

Shan Y, Phillen M, Lotfi A, Li SY, Bakis CE, Rahn CD, et al. (2009) Variable stiffness structures utilizing fluidic flexible matrix composites. *Journal of Intelligent Material Systems Structures* 20(4): 443–456.

Thill C, Etches J, Bond I, Potter K and Weaver P (2008) Morphing skins. *Aeronautical Journal* 112(1129): 117–139.

Xia M, Kemmochi K and Takayanagi H (2001a) Analysis of filament-wound fiber reinforced sandwich pipe under combined internal pressure and thermomechanical loading. *Composite Structures* 51: 273–283.

Xia M, Takayanagi H and Kemmochi K (2001b) Analysis of multi-layered filament-wound composite pipes under internal pressure. *Composite Structures* 53: 483–491.

Yin WL, Sun QJ, Zhang B, Liu JC and Leng JS (2008) Seamless morphing wing with SMP skin. *Advanced Materials Research* 47–50: 97–100.